Chinese Chemical Letters 36 (2025) 109590

Contents lists available at ScienceDirect

Chinese Chemical Letters

journal homepage: www.elsevier.com/locate/cclet

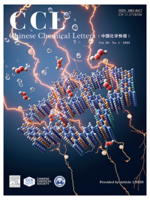

CoPSe nanoparticles confined in nitrogen-doped dual carbon network towards high-performance lithium/potassium ion batteries

Zhong-Hui Sun[a], Yu-Qi Zhang[a], Zhen-Yi Gu[b], Dong-Yang Qu[a,*], Hong-Yu Guan[a,*], Xing-Long Wu[b,*]

[a] *Guangdong Engineering Technology Research Center for Photoelectric Sensing Materials and Devices, c/o School of Chemistry and Chemical Engineering, Guangzhou University, Guangzhou 510006, China*
[b] *MOE Key Laboratory for UV Light-Emitting Materials and Technology, Northeast Normal University, Changchun 130024, China*

ARTICLE INFO

Article history:
Received 6 December 2023
Revised 19 January 2024
Accepted 29 January 2024
Available online 4 February 2024

Keywords:
Cobalt phosphoselenide
Lithium-ion batteries
Potassium-ion batteries
Reduced graphene oxide
Structural stability
Full cell

ABSTRACT

The metal ion batteries have gained widespread attention for wearable electronics due to their competitive energy density and long cycling life. Exploring the advanced anode materials is significant for next generation energy storage systems. However, severe electrode volume changes and sluggish redox kinetics are the critical problems for lithium/potassium ion batteries (LIBs/PIBs) towards large-scale applications. Herein, we prepare a novel anode material, which consists of reduced graphene oxide wrapping one-dimensional (1D) N-doped porous carbon nanotube with cobalt phosphoselenide (CoPSe) nanoparticles embedded inside them (rGO@CoPSe/NC). Benefited from the dual carbon decorations and ultrafine nanoparticles structure, it achieves a reversible capacity of 245 mAh/g at 5 A/g after 2000 cycles for LIBs and 215 mAh/g at 1 A/g after 500 cycles for PIBs. The pseudocapacitance and GITT measurements are used to investigate the electrochemical kinetics of rGO@CoPSe/NC for LIBs. In addition, the lithium ion full cell also shows good electrochemical performance when paired with high capacity $LiNi_{0.8}Co_{0.1}Mn_{0.1}O_2$ cathode. This work provides a feasible electrode design strategy for high-efficiency metal ion batteries based on multidimensional nanoarchitecture engineering and composition tailoring.

The use of fossil fuels has stimulated the growth of automobile industry, but it has also raised serious concerns about the environmental problems and non-renewable resource consumption [1]. In line with the goal of "carbon peak and neutrality", the development of renewable energy storage system has been regarded as a vital challenge for modern society [2]. Lithium ion batteries (LIBs), as the most advanced energy storage technology, have been extensively applied in various fields. However, the current LIBs still rely on commercial graphite as the dominant anodes. The low theoretical capacity (372 mAh/g) of graphite limits its further applications in LIBs. Therefore, it is essential to explore the alternative energy storage systems that use different chemical reaction mechanisms to significantly improve the specific capacity of the rechargeable batteries, using lithium, sodium, and potassium as charge carriers [3–6].

Transition metal selenides based on the conversion reactions have been extensively studied due to their high theoretical metal (Li, Na, K) ion storage capacity and abundant electronic structure features [6]. For example, $CoSe_2$ as a typical anode material for LIBs/PIBs that has superior capacity and fast ion diffusion kinetics [7,8]. However, their electrochemical performances are severely restricted by the inherent poor electrical conductivity, spontaneous aggregation and huge volume change during conversion reaction, leading to limited rate capabilities and structural collapse of the $CoSe_2$-based electrodes [9–11]. Therefore, many efforts have been devoted to boost the ion storage capability of $CoSe_2$-based anodes by micro/nano hierarchical hybrid structure, phase control, conductive network construction, and anion doping [12]. Recently, developing the ternary transition metal compounds becomes a favorable choice owing to multiple redox active sites induced by a third element [13–17]. In addition, vacancy engineering has been widely used to adjust the redistribution of electrons and tailor the physicochemical properties, generating extra active sites [18]. Ternary cobalt phosphoselenide (CoPSe) as an emerging electrode host perfectly integrated with the advantages of $CoSe_2$ and CoP, which possesses the regulated electronic structure and enhanced energy storage performances compared with its corresponding binary counterpart [19–21]. For example, Yang *et al.* synthesized CoPSe nanopar-

---

[*] Corresponding authors.
E-mail addresses: dyqu@gzhu.edu.cn (D.-Y. Qu), guanhy@gzhu.edu.cn (H.-Y. Guan), xinglong@nenu.edu.cn (X.-L. Wu).

https://doi.org/10.1016/j.cclet.2024.109590

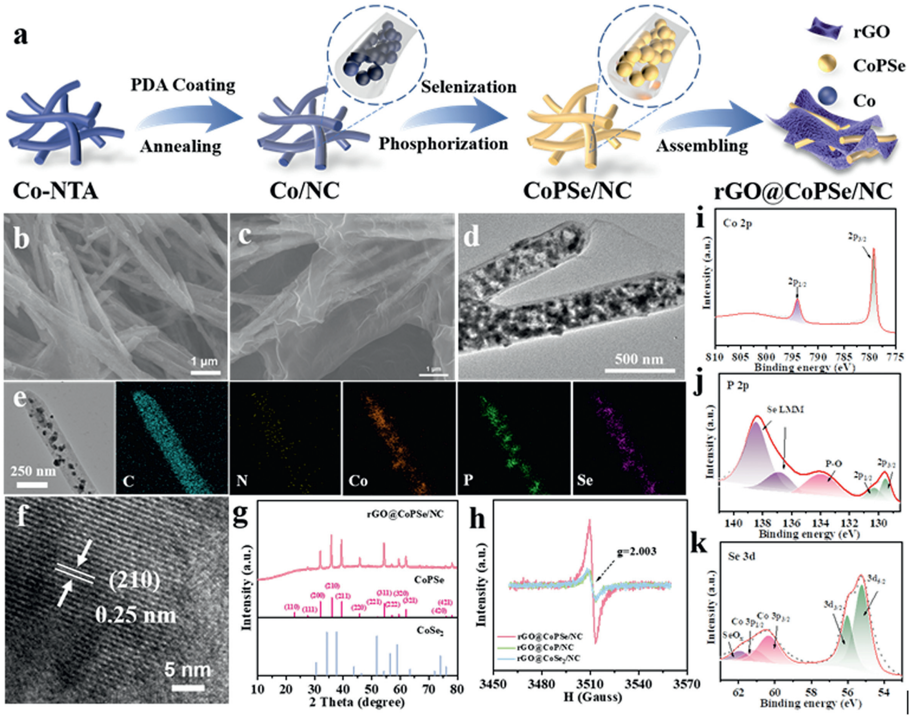

Fig. 1. (a) Scheme of the synthesis route of the rGO@CoPSe/NC composite. SEM images of (b) CoPSe/NC and (c) rGO@CoPSe/NC. (d) TEM image of rGO@CoPSe/NC. (e) TEM-EDX element mapping. (f) HRTEM, (g) XRD pattern, (h) EPR results for rGO@CoPSe/NC, rGO@CoP/NC, rGO@CoSe$_2$/NC. XPS spectra of (i) Co 2p, (j) P 2p, (k) Se 3d for the rGO@CoPSe/NC.

ticles embedded in the metal-organic framework (MOF)-derived N-doped carbon matrix exhibiting superior electrochemical performances for sodium/potassium ion batteries. However, to the best of our knowledge, the introduction of structure defect along with dual carbon conductive network decorations with CoPSe nanoparticles has been rarely reported until now.

Herein, we report the preparation of reduced graphene oxide wrapped CoPSe nanoparticles embedded in the N-doped carbon nanotube (rGO@CoPSe/NC) by one-pot *in situ* phosphorization/selenization reactions. The fabricated rGO@CoPSe/NC composites integrate the advantages of each component: (1) The introduction of P atom into CoSe$_2$ phase endows CoPSe enhanced theoretical alkali ion storage capacity compared with its counterpart of CoSe$_2$. (2) Partial substitution of P atoms for Se atoms in CoSe$_2$ lattice with anion vacancies will provide more active sites and simultaneously improve electronic conductivity as well as boost the electrochemical reaction kinetics. (3) Dual conductive carbon network confined CoPSe nanoparticles further accelerates the transport kinetics of ions and electrons and prevents the aggregation of CoPSe nanoparticles, which ensures the structural stability during the charge and discharge processes. Benefiting from these advantages, the rGO@CoPSe/NC exhibits excellent Li$^+$/K$^+$ ions storage performance with high capacity, stable cycling life, and high rate capability.

Fig. 1a shows the synthesis process of the rGO@CoPSe/NC composite. First, Co-NTA nanotubes with an average diameter of 200 nm are synthesized by a facile solvothermal reaction according to the reported report (Fig. S1a in Supporting information) [22]. Then, the Co-NTA nanotubes are pyrolyzed into Co metal nanoparticles confined in N-doped carbon nanotubes (Co/NC) under an Ar atmosphere (Figs. S1b and S2 in Supporting information). Subsequently, the Co/NC is synchronously phosphorized and selenized to obtain CoPSe/NC nanoparticles in a vacuum quartz tube (Fig. 1b). Finally, the CoPSe/NC nanotubes are assembled with reduced graphene oxide nanosheets to form rGO@CoPSe/NC composites through strong electrostatic interaction (Fig. 1c). TEM image in Fig. 1d shows CoPSe nanoparticles are homogeneously confined in the N-doped carbon nanotubes. TEM-based energy dispersive X-ray spectroscopy mappings show that each element is uniformly distributed throughout the entire nanotube (Fig. 1e). The high-resolution transmission electron microscopy (HRTEM) image of CoPSe shows well-defined lattice fringe spacings of 2.50 Å point to the (210) plane of the cubic-phase CoPSe (Fig. 1f) [21]. The X-ray diffraction (XRD) pattern of rGO@CoPSe/NC in Fig. 1g can be well indexed to the simulated pattern of cubic-CoPSe. Electron paramagnetic resonance (EPR) analysis is performed to verify the detailed defect and vacancy features for the as-prepared samples. As can be found in Fig. 1h, a characteristic signal at *g* value of 2.003 resulting from anion vacancy. It can be clearly seen that rGO@CoPSe/NC displays the highest vacancy content, which may be caused by two anions coexist in the lattice. The chemical composition and elemental valences of rGO@CoPSe/NC are carried out by X-ray photoelectron spectroscopy (XPS). The survey spectrum indicates the presence of C, N, Co, P, Se O elements (Fig. S3a in Supporting information). The existence of O element derived from absorbed oxygen on the surface of the rGO@CoPSe/NC. High resolution Co 2p XPS spectrum (Fig. 1i) shows two peaks located at 779.3 and 794.2 eV corresponding to the 2p3/2 and 2p1/2 of Co^{3+}, respectively. High resolution P 2p XPS spectrum in Fig. 1j illustrates the two dominating peaks at 130.3 and 129.5 eV are assigned to 2p$_{3/2}$ and 2p$_{1/2}$ orbitals, respectively. The peak at 133.8 eV is assigned to the P–O bonds [23]. In addition, the peak located at 138.5 eV is the Se Auger emission line. High resolution Se 3d XPS spectrum in Fig. 1k shows three peaks located at 56.3, 55.5 and 61.6 eV, corresponding to the Se 3d$_{3/2}$, Se 3d$_{5/2}$ and Se–O, respectively [24]. Moreover, the Co 3p$_{1/2}$ (60.1 eV) and Co 3p$_{3/2}$ (58.9 eV) spectra are detected in the Se 3d XPS spectrum [25]. High-resolution C 1s spectrum is split into two peaks at 284.5 and 285.6 eV (Fig. S3b in Supporting information), which correspond to C–C, and C=N, respectively [18]. As for the N 1s spectra (Fig. S3c in Supporting informa-

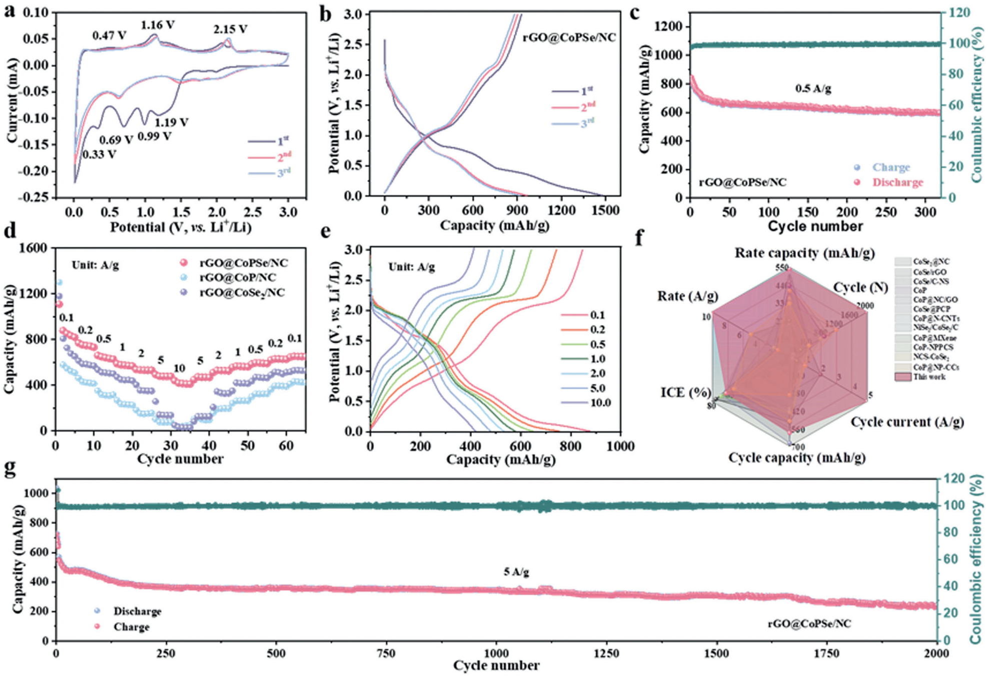

Fig. 2. Electrochemical performance of rGO@CoPSe/NC in LIBs. (a) CV curves at a scan rate of 0.1 mV/s. (b) GCDs at 0.1 A/g. (c) Cycling performance at 0.5 A/g. (d) Rate capability at various current densities. (e) The corresponding GCD curves. (f) Comparison of rate capability with reported metal chalcogenides. (g) Long-term cyclic performance at the current density of 5 A/g.

tion), four peaks are deconvoluted, which ascribe to the graphitic N (401.5 eV), pyrrolic N (400.9 eV), Co-N2 (399.2 eV), and pyridinic-N (397.8 eV) [26]. Raman spectra show the two peaks at 1323 and 1578 cm^{-1} corresponding to D and G bands with intensity ratio (I_D/I_G) of are 1.14, which are higher than that of rGO@CoP/NC and rGO@CoSe$_2$/NC (Fig. S4 in Supporting information), suggesting the existence of rich structural defects in rGO@CoPSe/NC. The rGO@CoPSe/NC composite shows a Brunauer–Emmett–Teller surface area of 122.4 m^2/g with a pore volume of 0.39 cm^3/g (Fig. S5 in Supporting information). Moreover, the pore size distribution curve indicates hierarchically porous feature with high proportion of mesopores. Previous studies have shown that the mesopores enable fast ion transport for improving rate capability and alleviate volume expansion for maintaining cycling stability [27]. For comparison, the rGO@CoSe$_2$/NC and rGO@CoP/NC are also synthesized. As shown in Figs. S6a and b (Supporting information), their morphologies are the same with that of rGO@CoPSe/NC. The XRD patterns (Figs. S6c and d in Supporting information) and XPS survey spectra (Figs. S6e and g in Supporting information) further confirm their successful preparation of the rGO@CoSe$_2$/NC and rGO@CoP/NC.

The lithium storage properties of the prepared samples are evaluated by assembling 2032-type coin cells, where the lithium metal foils are used as counter electrodes and the as-prepared electrodes are served as working electrode. The initial three cyclic voltammetry (CV) curves of rGO@CoPSe/NC at a scan rate of 0.1 mV/s in the potential range of 0.01–3.00 V are shown in Fig. 2a. An irreversible cathodic peak at 1.19 V observed at the 1st cycle and subsequently vanishes in the following cycles, which could be due to the formation of solid-electrolyte interphase (SEI) layer from the electrolyte decomposition and reaction on the lithium anode surface. In addition, the three peaks at 0.99, 0.69, 0.34 V in the cathodic curve correspond to the different stages of lithium ion intercalation reactions and conversion reaction, forming Co, P and Li_2Se phases [28,29]. A sharp cathodic peak near 0.02 V is due to the alloying reaction of P and Li$^+$ to yield Li_3P coupling with Li$^+$ insertion into carbon framework [30]. During the anodic process, all the anodic curves overlap well, a slightly hump located at 0.47 V represents the dealloying process of Li_3P to P, and the other two peaks situated at 1.16 and 2.15 V possibly correspond to the conversion reaction from Co, Li_3P and Li_2Se to Li_xCoSe_2, as well as delithiation of Li_xCoSe_2 to $CoSe_2$, respectively [31]. Next, P and $CoSe_2$ as active materials could provide capacity in subsequent cycles. These results are consistent with the previously reported CoPSe anodes and CoPS [13]. In the subsequent cycles, the well overlapped CV curves indicate that good reversibility on the lithiation and delithiation processes. Interestingly, compared with the CV and galvanostatic charge/discharge (GCD) curves of the rGO@CoSe2/NC electrode (Fig. S7 in Supporting information), it is noted that the incorporation of P into $CoSe_2$ lowers the redox potentials of the rGO@CoPSe/NC electrode, which enhances the energy density of the rGO@CoPSe/NC-based full cell with a specific cathode material [21].

The GCD curves of rGO@CoPSe/NC electrode for the initial three curves at a current density of 0.1 A/g are shown in Fig. 2b, the charge/discharge plateaus of which are well consistent with the CV results. A high reversible capacity of 930 mAh/g can be obtained in comparison of rGO@CoSe$_2$/NC (700 mAh/g). The cycling performance is further displayed in Fig. 2c, where it maintains a discharge capacity of 600 mAh/g after 318 cycles at 0.5 A/g. The rate capability of the three electrodes is investigated at various current rates ranging from 0.5 A/g to 10 A/g (Figs. 2d and e). The rGO@CoPSe/NC delivers the most superior reversible capacity of 432 mAh/g even at the current density of 10 A/g. When the current density returns to 0.1 A/g, a decent capacity of 700 mAh/g can be recovered. However, both rGO@CoSe$_2$/NC and rGO@CoP/NC electrodes exhibit inferior rate capability at the same current rate. The severe deterioration of the both electrodes could be attributed to the exfoliation of the electrode materials from the current collector during the repeated cycling of Li$^+$ ion intercalation/deintercalation (Fig. S8 in Supporting information). The cyclic performances of three samples are compared as shown in Fig. S9 (Supporting

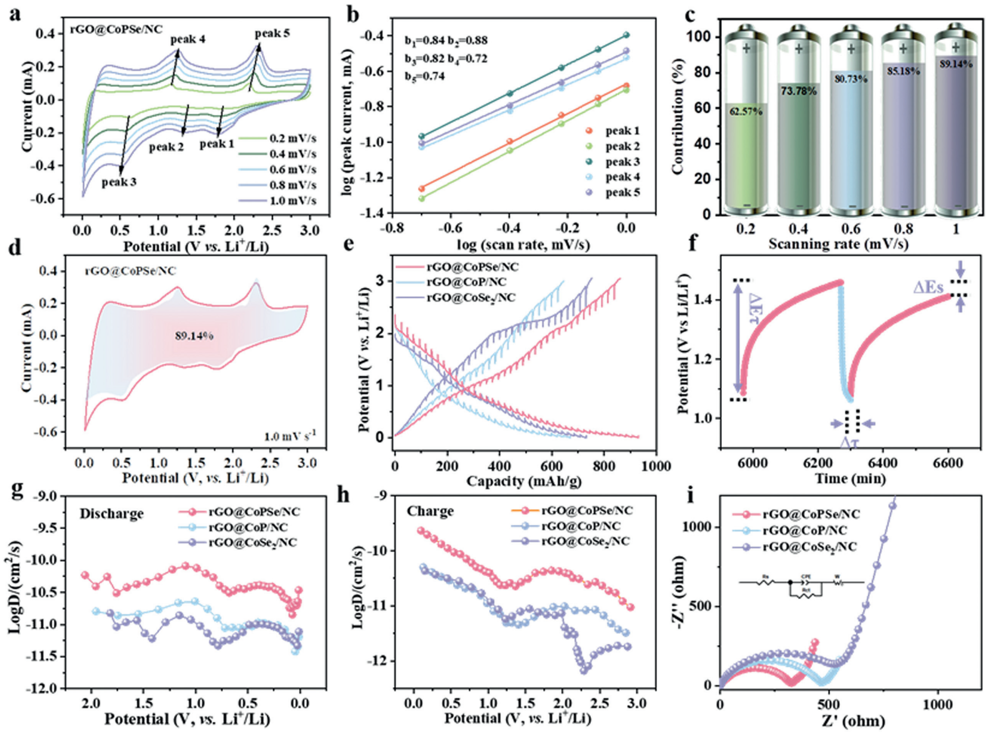

Fig. 3. (a) CV curves at scan rates from 0.2 mV/s to 1.0 mV/s. (b) *b*-value determined from the relation between log*i* and log*v*. (c) Normalized capacitive contribution for Li storage at different scan rates. (d) Capacitive contribution at 1.0 mV/s. (e) GITT curves. (f) Voltage response over time during a single current pulse. (g, h) The corresponding Li^+ diffusion coefficient at discharge and charge process, (i) Nyquist plots of rGO@CoPSe/NC, rGO@CoSe$_2$/NC and rGO@CoP/NC.

information), further indicating the robust structural stability of rGO@CoPSe/NC. Notably, the rate capability of rGO@CoPSe/NC is superior to most reported metal chalcogenides for LIBs (Fig. 2f), which is attributed to the unique structure design and dual carbon high electronic conductivity network decoration [32–43]. Furthermore, the long cycling performances of rGO@CoPSe/NC are investigated at 5 A/g, respectively. As expected, it can achieve a higher reversible capacity of 245 mAh/g with high coulombic efficiency over 2000 cycles (Fig. 2g). In addition, the as-prepared samples are also applicable in the Na^+ and K^+ ions storage. Among them, rGO@CoPSe/NC shows excellent charge storage performance, the high reversible capacity can be obtained at various current densities. Moreover, rGO@CoPSe/NC also has superior cycling stability for 500 cycles (Fig. S10 in Supporting information).

To have a deep insight into the origins of enhanced rate performance for LIBs, the electrochemical kinetics of rGO@CoPSe/NC electrodes are studied by the CV analysis at various scan rates (Fig. 3a). rGO@CoPSe/NC shows a well-preserved CV curves shape with the increase of scan rate from 0.2 mV/s to 1.0 mV/s, implying a negligible electrode polarization during charge and discharge processes. Based on the previous studies, the relationship between current (i) and scan rate (v) can be described using the equation: $i = av^b$, where a and b are adjustable parameters and can be used to describe the relationship of v and i. Specifically, when the value of b is close to 1, the capacitance process is dominated, while it approaches to be 0.5 for the diffusion-controlled process [44,45]. The calculated b-values of redox peaks for the rGO@CoPSe/NC are in the range from 0.74 to 0.88 for both cathodic and anodic peak currents, which are higher than that of rGO@CoSe$_2$/NC and rGO@CoP/NC electrodes, suggesting a dominant ultrafast surface charge storage behavior in Li^+ storage mechanism (Fig. 3b, Figs. S11a, b, d and e in Supporting information). The contribution of capacitance can be quantified by equation: $i = k_1 v + k_2 v^{1/2}$, where $k_1 v$ and $k_2 v^{1/2}$ correspond to the contribution of pseudocapacitance and diffusion-controlled capacitance, respectively [46]. Fig. 3c together with Figs. S11c and f (Supporting information) present the detailed pseudocapacitive percentage at 1.0 mV/s, it is 89.14% for rGO@CoPSe/NC, 81.67% for rGO@CoSe$_2$/NC, and 70.49% for rGO@CoP/NC, indicating the surface capacitive behaviors of three electrodes are dominating at this scan rate. Furthermore, with the increase of scan rate, there is an increase in capacitance contribution and rGO@CoPSe/NC has a higher capacitive contribution compared with two reference electrodes, further verifying that the capacitive property is enhanced by the presence of ternary metal phosphoselenide (Fig. 3d).

The galvanostatic intermittent titration technique (GITT) tests are used to *in situ* characterize the electrochemical reaction kinetics of the three electrodes during lithiation and delithiation processes. The GITT profiles of the three electrodes at a current density of 50 mA/g are presented in Fig. 3e, and the voltage variation during a single current pulse for rGO@CoPSe/NC is displayed in Fig. 3f. The detailed Li^+ diffusion coefficient (D_{Li^+}) is explicitly elaborated in Supporting information. It can be found that the D_{Li^+} values of three electrodes manifest similar evolution tendency and its range fluctuates between $10^{-9.5}$ cm^2/s and 10^{-12} cm^2/s during the discharge and charge process (Figs. 3g and h). Notably, the rGO@CoPSe/NC electrode shows the highest Li^+ diffusion coefficients amongst three electrodes for both Li^+ insertion and extraction processes, indicating the boosted ion-migration ability and fast reaction kinetics. The electrochemical reaction kinetics are further investigated by EIS measurements. The Nyquist plots show a high-frequency arc and a low-frequency linear portion (Fig. 3i), which correspond to the R_{ct} and the Z_w, respectively. The R_{ct} values of three samples are shown in Table S1 (Supporting information). The reduced impedance value of rGO@CoPSe/NC is attributed to the synergistic effects of CoPSe nanoparticles and dual carbon conductive work, which facilitate the electron transfer.

Research on rGO@CoPSe/NC anode based full-cell is believed to be significant for practical LIBs application. Before assembling the full cell (Fig. 4a), all the rGO@CoPSe/NC anodes proceed chemical

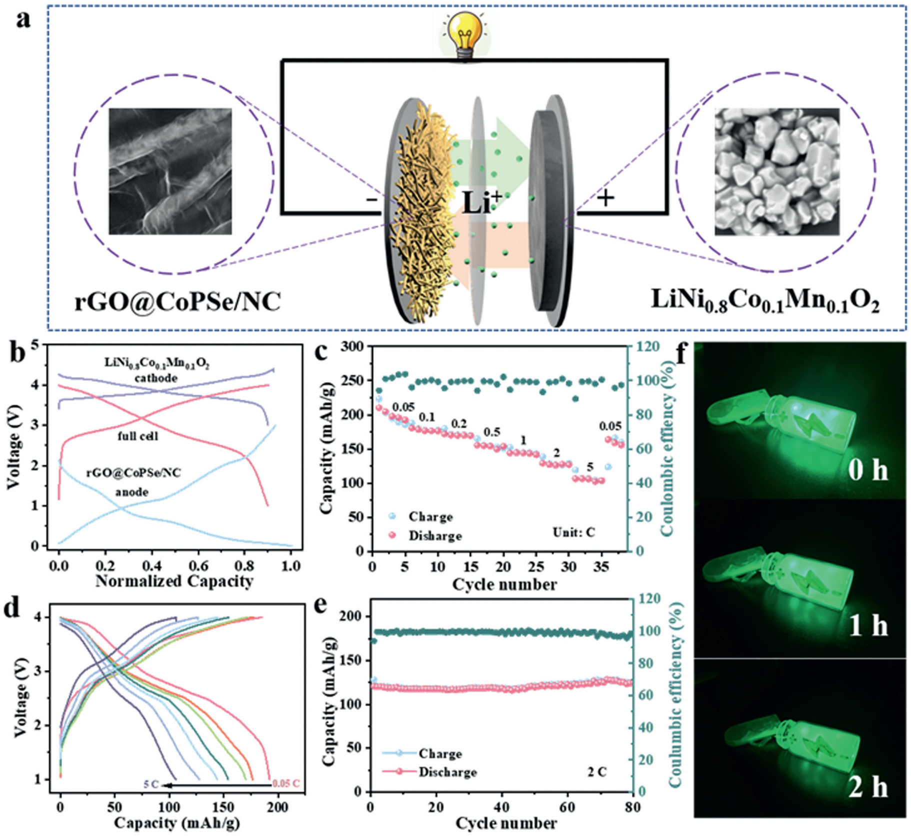

Fig. 4. (a) Schematic illustration of Li-ion full cell. (b) GCD curves of rGO@CoPSe/NC anode, $LiNi_{0.8}Co_{0.1}Mn_{0.1}O_2$ cathode, and corresponding full cell at a current density of 0.1 C. (c) Rate capability at various current densities from 0.05 C to 5 C (1 C = 100 mA/g). (d) GCD curves at different current densities. (e) Cycling performance at 2 C. (f) The application of full cell for powering green LED bulbs.

presodiation to stabilize the surface structure and reduce the irreversible capacity loss. The structural characterization and electrochemical properties of $LiNi_{0.8}Co_{0.1}Mn_{0.1}O_2$ in the voltage range of 3.0–4.4 V are presented in Fig. S12 (Supporting information), manifesting outstanding lithium storage performance. Fig. 4b demonstrates the typical GCD profiles of the $LiNi_{0.8}Co_{0.1}Mn_{0.1}O_2$ cathode, rGO@CoPSe/NC anode, and full cell, indicating that the full cell assembled by rGO@CoPSe/NC anode and $LiNi_{0.8}Co_{0.1}Mn_{0.1}O_2$ cathode are well matched. Moreover, the full cell also shows superior energy storage performance in terms of rate capability and cycle performance. As shown in Fig. 4c, when the current density increased to 5 C, the full cell delivers a high capacity of 107 mAh/g with obvious charge and discharge plateaus (Fig. 4d). The cyclic stability of full cell is exhibited in Fig. 4e, the capacity retention can achieve as high as 85% of initial capacity after 80 cycles at 2 C. The full cell can lighten LED bulbs for 2 h without any brightness decay in Fig. 4f, illustrating the practical application for the as-designed rGO@CoPSe/NC anode.

In summary, CoPSe nanoparticles embedded in N-doped carbon nanotubes and subsequently wrapped in rGO conductive network are developed *via in situ* synchronous phosphorization/selenization reactions. The CoPSe nanoparticles with rich anion vacancies can facilitate the Li^+/K^+ insertion and provide more active sites and decrease the ion diffusion barrier. The rGO layer and porous carbon matrix derived from organic ligand pyrolysis can effectively alleviate the volume change and offer high-conductivity networks for CoPSe and accelerate the migration speed of Li^+/K^+ during cycling. With the above merits, the rGO@CoPSe/NC as anodes hold excellent charge storage properties in terms of capacity and rate capability. Moreover, the constructed Li-ion full cell based on the rGO@CoPSe/NC anode and the $LiNi_{0.8}Co_{0.1}Mn_{0.1}O_2$ cathode can achieve a high energy density. The present work not only sheds light on an innovative anode material construction for Li^+/K^+ ion batteries, but also resolves the volume expansion and sluggish kinetics that often occurs in metal ion batteries systems.

Declaration of competing interest

The authors declare that they have no known competing financial interests or personal relationships that could have appeared to influence the work reported in this paper.

Acknowledgments

This work is financially supported by the National Natural Science Foundation of China (No. 22204028), Young Talent Support Project of Guangzhou Association for Science and Technology (No. QT-2023-003), Guangdong Basic and Applied Basic Research Fund Project (No. 2022A1515110451), Guangzhou University Graduate Student Innovation Ability Cultivation Funding Program (No. 2022GDJC-M06), Science and Technology Projects in Guangzhou (Nos. 202201010245, 2023A03J0029), and Double-Thousand Talents Plan of Jiangxi Province (No. jxsq2023102005).

Supplementary materials

Supplementary material associated with this article can be found, in the online version, at doi:10.1016/j.cclet.2024.109590.

References

[1] X. Liang, J.Y. Hwang, Y.K. Sun, Adv. Energy Mater. 13 (2023) 2301975.
[2] B. Chen, S. Sui, F. He, et al., Chem. Soc. Rev. 52 (2023) 7802–7847.

[3] Z.H. Sun, D.Y. Qu, D.X. Han, et al., Adv. Mater. 36 (2023) 2308987.
[4] F. Zhou, R.H. Wang, S.C. He, et al., Adv. Funct. Mater. 33 (2023) 2211124.
[5] A. Innocenti, H. Adenusi, S. Passerini, InfoMat 5 (2023) 12480.
[6] Z.Y. Gu, J.Z. Guo, J.M. Cao, et al., Adv. Mater. 34 (2022) 2110108.
[7] J. Yang, H. Gao, S. Men, et al., Adv. Sci. 5 (2018) 1800763.
[8] C.A. Etogo, H. Huang, H. Hong, et al., Energy Storage Mater. 24 (2020) 167–176.
[9] Z. Sun, Z. Gu, W. Shi, et al., J. Mater. Chem. A 10 (2022) 2113–2121.
[10] Z.K. Yang, X. Liu, F. Ren, J. Alloys. Compd. 969 (2023) 172227.
[11] J.C. Ren, H. Zhu, Y.J. Fang, et al., Carbon Neutralization 2 (2023) 339–377.
[12] Z. Sun, X.L. Wu, J. Xu, et al., Small 16 (2020) 1907670.
[13] W. Zhao, X. Ma, L. Gao, et al., Adv. Mater. 36 (2023) 2305190.
[14] H.Y. Lu, R.L. Hou, S.Y. Chu, et al., Acta Phys. Chim. Sin. 7 (2023) 2211057.
[15] M.L. Xu, M.C. Liu, Z.H. Yang, et al., Acta Phys. Chim. Sin. 3 (2023) 2210043.
[16] B.C. Chen, X. Lu, H.Y. Zhong, et al., J. Mater. Chem. A 10 (2022) 25671–25682.
[17] S.H. Shishavan, M.N. Samani, Energy Storage Mater. 39 (2021) 96–107.
[18] T. Yang, M. Fang, J. Liu, et al., Adv. Funct. Mater. 32 (2022) 2205880.
[19] Y. Wu, Z. Wang, Z. Wang, et al., Energy Storage Mater. 57 (2023) 180–194.
[20] Y.Z. Zhao, C.Y. Chen, W.Y. Liu, Acta Phys. Chim. Sin. 8 (2023) 2211017.
[21] Y. Feng, M. Xu, T. He, et al., Adv. Mater. 33 (2021) 2007262.
[22] Q. Xiao, Q. Song, K. Zheng, et al., Nano Energy 98 (2022) 107326.
[23] D. Zhao, R. Zhao, S. Dong, et al., Energy Environ. Sci. 12 (2019) 2422–2432.
[24] S. Xiao, X. Li, W. Zhang, et al., ACS Nano 15 (2021) 13307–13318.
[25] X. Hu, Y. Liu, J. Chen, et al., Adv. Energy Mater. 9 (2019) 1901533.
[26] J. Chen, Y. Cheng, Q. Zhang, et al., Adv. Funct. Mater. 31 (2020) 2007158.
[27] Z. Cao, J. Cui, D. Yu, et al., Adv. Funct. Mater. 33 (2023) 2306862.
[28] Z. Liu, S. Yang, B. Sun, et al., Angew. Chem. Int. Ed. 57 (2018) 10187–10191.
[29] X. Hu, X. Liu, K. Chen, et al., J. Mater. Chem. A 7 (2019) 11016–11037.
[30] K. Guo, B. Xi, R. Wei, et al., Adv. Energy Mater. 10 (2020) 1902913.
[31] J. Yang, Y. Zhang, C. Sun, et al., Nano Res. 9 (2016) 612–621.
[32] Y. Wang, Y. Wu, L. Liu, et al., Solid State Ionics 370 (2021) 115747.
[33] Q. Wang, M. Hou, D. Liu, et al., J. Alloys. Compd. 864 (2021) 158099.
[34] L. Cui, H. Qi, N. Wang, et al., Nanotechnol. Rev. 11 (2021) 244–251.
[35] X. Xu, J. Liu, R. Hu, et al., Chemistry 23 (2017) 5198–5204.
[36] S. Sun, T. Xie, S. Tao, et al., Energy Technol. 8 (2019) 1901089.
[37] J. Li, D. Yan, T. Lu, et al., Chem. Eng. J. 325 (2017) 14–24.
[38] M. Chen, P. Zeng, Y. Zhao, et al., Front. Mater. Sci. 12 (2018) 214–224.
[39] H. Liu, Y. Lin, Y. Wu, et al., J. Mater. Sci. 32 (2021) 15059–15068.
[40] H. Zong, L. Hu, Z. Wang, et al., Chem. Eng. J. 416 (2021) 129102.
[41] J. Bai, B. Xi, H. Mao, et al., Adv. Mater. 30 (2018) e1802310.
[42] B. Li, H. Hu, H. Hu, et al., Electrochim. Acta 370 (2021) 137717.
[43] G.H. Lee, Y. Seon Kim, M.C. Sung, et al., Appl. Surf. Sci. 555 (2021) 149716.
[44] J.Z. Guo, Z.Y. Gu, X.X. Zhao, et al., Adv. Energy Mater. 9 (2019) 1902056.
[45] X. He, T. Wang, L. Tian, et al., Nano Res. 17 (2024) 4006–4015.
[46] H. Lei, H. Wang, B. Cheng, et al., Small 19 (2023) 2206340.